Supplementary Information: Effects of surface treatments on flux tunable transmon qubits

M. Mergenthaler,[1,*] C. Müller,[1] M. Ganzhorn,[1] S. Paredes,[1] P. Müller,[1] G. Salis,[1]
V.P. Adiga,[2] M. Brink,[2] M. Sandberg,[2] J.B. Hertzberg,[2] S. Filipp,[1] and A. Fuhrer[1]

[1]*IBM Quantum, IBM Research Europe - Zurich,*
Säumerstrasse 4, 8803 Rüschlikon, Switzerland
[2]*IBM Quantum, IBM T.J. Watson Research Center,*
Yorktown Heights, NY 10598, USA

(Dated: September 20, 2021)

CONTENTS

I. SUPPLEMENTARY NOTES ON EXPERIMENTAL SETUP/PROCEDURE

The measured samples each consist of four frequency tunable transmon qubits connected to a single transmission line through frequency multiplexed $\lambda/2$-resonators, as illustrated in Supplementary Fig. 1. The devices are fabricated on an intrinsic high-resistivity Si substrate, where the resonators and qubit capacitors are made from Nb. The SQUID loops of the qubits are fabricated in the last step via double angle evaporation of Al, see Ref. [1] for details. In total we measure four nearly identical chips from the same fabrication die and analyse the impact of surface treatments on these. Two chips at a time are wire-bonded to a multilayer PCB and mounted in a copper package designed to sustain UHV loading of the package. The sealing of the package and the surface treatments are performed in a specifically designed UHV chamber [2]. Two externally mounted coils provide the magnetic flux necessary for frequency tuning of the transmon qubits and allow independent frequency adjustment of one qubit on each chip at the same time. In this way, we always measure two qubits simultaneously in a bottom-loading dilution refrigerator with a sample base temperature of ~ 20 mK.

---

* mme@zurich.ibm.com

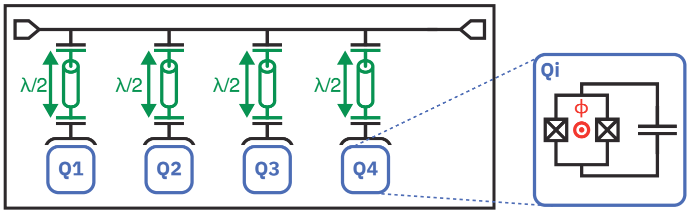

Supplementary Figure 1. Schematic of the measured qubit chips. Four lambda half resonators (green) are addressed via a common transmission line (black) and capacitively coupled to frequency tunable transmon qubits (blue). Inset: Circuit schematic of frequency tunable transmon qubit including applied external magnetic flux Φ (red).

After the cooldown of the samples the magnetic flux dependence of the 8 lambda half resonators is measured first in order to determine the flux period with the smallest offset. This is important in order not to heat the fridge with excessive coil currents. Spectroscopy measurements are performed with a 4-channel vector network analyser and time-domain measurements via up- and down-conversion in a heterodyne detection setup. All coherence measurements are started after a minimum of 24 h with the fridge at base temperature, leaving enough time for thermalisation of the qubits. Initial characterisation of the individual qubits involves measuring their flux-dependent transition frequency, f_{01}, to determine the qubits' sweet spot. At the sweet spot the anharmonicity α is determined, $\alpha = 320-350$ MHz (chip dependent). Additionally, at the sweet spot the qubit temperature is determined to be $T_{\text{Qubit}} \sim 45-60$ mK, showing good thermalisation and isolation of the qubits. To determine T_{Qubit} we measure the qubit excited state population by Rabi driving at ω_{12} with and without an initial π-pulse at ω_{01}.

II. SUPPLEMENTARY NOTES ON SURFACE TREATMENTS AND COMPARISONS

A challenge in studying the impact of surface treatments is the comparison of relevant coherence parameters without and with a given treatment. Ideally this would be done with a set of 100 qubits that are measured both clean (directly after fabrication) in multiple cooldowns and then after the treatment with otherwise identical conditions. Investigations on the interplay of different treatments (e.g. UV and NH_3 or Ne ion milling and NH_3) would require further separate experiments with different reference measurements. In order to limit our experiments to a more manageable scale, we reused our chips by exposing them to successively more involved treatments (e.g. no treatment, just UHV loading, UV exposure and UHV loading, UV exposure and neon ion milling and UHV loading, ...) and then made comparisons between consecutive cooldowns. In addition, we also used the ability to cover one chip in the package with a copper foil allowing a side by side comparison of e.g. ion irradiated qubits and non-irradiated qubits. This has the advantage that conditions such as mounting of the chips in the package did not change in successive measurements, however, it has the clear drawback that some comparisons are done with changed coherence parameters in regard to those directly after fabrication. Supplementary Table I gives a more detailed description of the treatment parameters that we used. Generally all ion bombardment treatments were done in a background pressure of $1.0e^{-4}$mbar. The NH_3 backfills were done at a pressure of $5e^{-3}$mbar, closing the package after pumping down to a pressure of $1e^{-6}$mbar. The pressure P is the pressure of the chamber when closing the package.

Nr.	Symb.	Label	#Qubits	P [mBar]	Treatment parameters
(i)	●	UHV	12	$< 1e^{-9}$	-
(ii)	×	UV	22	$< 1e^{-9}$	λ ~140 nm, 10 min
(iii)	◊	UV + NH_3	8	$1e^{-6}$	UV, 10 min; NH_3 @ $5e^{-3}$ mBar
(iv)	○	R	8	$< 1e^{-9}$	two consecutive cooldowns
(v)	△	Ne	2	$< 1e^{-9}$	20 min, $U_{\mathrm{acc}} = 0.75$ kV
(vi)	⬠	Ne+NH_3	4	$< 1e^{-9}$	40 min, $U_{\mathrm{acc}} = 1.25$ kV; NH_3 @ $5e^{-3}$ mBar
(vii)	★	SF_6	4	$< 1e^{-9}$	20 min, $U_{\mathrm{acc}} = 1.25$ kV
(viii)	□	SF_6/SF_6	12	$< 1e^{-9}$	20 min, $U_{\mathrm{acc}} = 1.25$ kV

Supplementary Table I. Treatment parameters and description of the two treatment conditions that were compared.

III. SUPPLEMENTARY NOTES ON FLUX NOISE ANALYSIS

For the flux noise analysis in Fig. 3(c)+(d) of the main text we use flux dependent measurements of $\Gamma_2^{\mathrm{e}} = \Gamma_{2,SS}^{\mathrm{e}} + \Gamma_{2,\Phi}^{\mathrm{e}}$ in order to extract a 1/f and a constant (broad band)

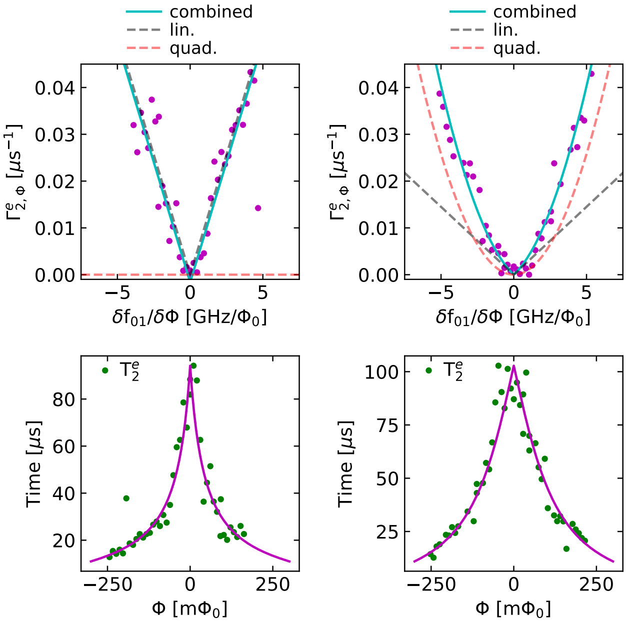

Supplementary Figure 2. Flux dependent echo decay rate $\Gamma^{\mathrm{e}}_{2,\Phi}$ and echo decay time T_2^{e} as a function of the flux sensitivity D_Φ for two different qubits in the same cooldown. The solid lines are fits to the using the model described in the text. The dashed lines show the linear and quadratic contributions to $\Gamma^{\mathrm{e}}_{2,\Phi}$ as extracted from the polynomial fit.

flux-noise component (see Fig. 2 of the main text). We use a standard analysis as described below and similar to that in Refs. [3–6] in order to compare our data with that of others. This analysis has the advantage that it singles out the impact of flux noise (through the explicit flux dependence) and is very robust for data of a wide range of noise levels. However, it is also a simple model in that it assumes only two spectral components (1/f and constant) and is only sensitive to noise in a frequency window given by the filter function of the echo measurement [3, 7]. In this limited frequency range it is not possible to separate out small changes in noise exponent as compared to changes in relative amplitude between the different noise components. In principle an increase in $1/f$-noise could also be due to a reduction in the noise exponent α, were we to assume a frequency dependence $1/f^{\alpha}$ instead of $1/f$. However, we do not take this into account in our analysis. In Supplementary Fig. 2 we show two cases of the full flux dependence of $\Gamma^{\mathrm{e}}_{2,\Phi}$ and T_2^{e} respectively. The two plots on the left give an example where 1/f noise dominates and the two on the right where broadband noise dominates the noise spectrum. As can be seen from these, the shape of the flux dependent curves clearly changes. Additionally, we also show four comparison plots of $\Gamma^{\mathrm{e}}_{2,\Phi}$ at four

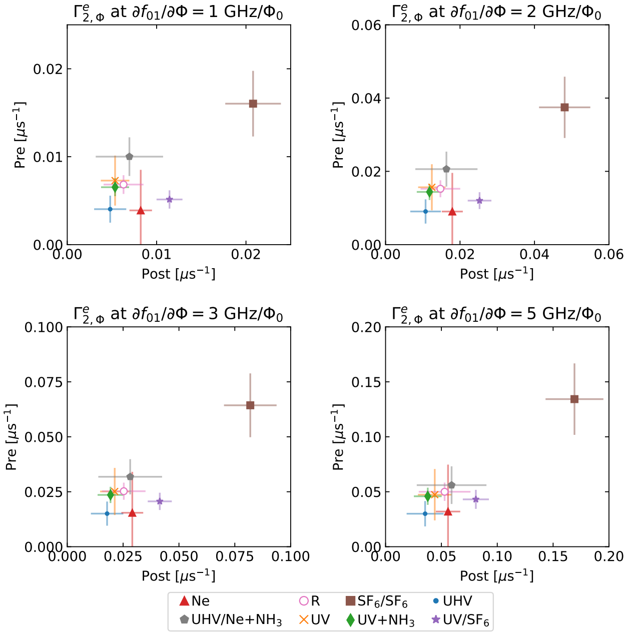

Supplementary Figure 3. Mean value of $\Gamma^e_{2,\Phi}$ at four different flux sensitivties $D_\Phi = \delta f_{01}/\delta\Phi$. Error bars indicate the standard deviation of values measured across multiple qubits.

different flux sensitivities away from the sweet spot in Supplementary Fig. 3. From this we can see a general confirmation of our conclusion that ion treatments increase flux noise except when a passivation with NH_3 is present. For the UV treatments the improvement in the 1/f component of the noise is roughly canceled by the increase in broadband noise at a flux sensitivity of $D_\Phi = 5$ GHz$/\Phi_0$ (lower right plot). In contrast, at the same flux sensitivity a slight net improvement is observed for a UV treatment with NH_3 passivation. However, at lower flux sensitivity D_Φ there is a net improvement of $\Gamma^e_{2,\Phi}$ for both UV treatments. For the neon treatment with NH_3 passivation the same is true and again the net impact of the treatment on flux noise is very small far away from the sweet spot but significant near the sweet spot.

A. Flux-noise filter function for echo experiments

As discussed previously, echo experiments filter away the low frequency noise components. It is thus interesting to calculate the filter function that determines the flux-noise sensitivity. Following Ref. [8], we write the decay function for the density matrix off-diagonal entries as $\sim e^{-\chi(t)}$, for the total evolution time t. The decay function $\chi(t)$ is given by the spectral function of the environment $S(\omega)$ and depending on the pulse sequence as [8, 9]

$$\chi(t) = \int_{-\infty}^{\infty} \frac{d\omega}{2\pi} \frac{S(\omega)}{\omega^2} F_n(\omega t) = t^2 \int_0^{\infty} \frac{d\omega}{\pi} S(\omega) g_n(\omega t) \tag{1}$$

This definition of the decay function $\chi(t)$ is by a factor π different from that in Refs. [7, 9, 10] (see notes on units below). $F_n(\omega t)$ and $g_n(\omega t)$ are two definitions for filter functions for a sequence with n π-pulses [7, 8] defined by

$$F_n(\omega t) = \frac{1}{2} \left| \sum_{k=0}^{n} (-1)^k \left(\mathrm{e}^{\mathrm{i}\omega t_{k+1}} - \mathrm{e}^{\mathrm{i}\omega t_k} \right) \right|^2 \tag{2}$$

$$g_n(\omega t) = \frac{F_n(\omega t)}{(\omega t)^2} \tag{3}$$

Here $t_k = t * k/(n+1)$ is the time at which the k-th pulse is applied in the pulse train (including the $\pi/2$- pulses at the beginning and end). For Ramsey and Echo sequences, one can simplify [9] this to

$$\begin{aligned} F_0(\omega t) &= 2\sin^2\frac{\omega t}{2}, \quad F_1(\omega t) = 16\sin^4\frac{\omega t}{4}\,, \\ g_0(\omega t) &= 2\,\mathrm{sinc}^2\frac{\omega t}{2}, \quad g_1(\omega t) = \mathrm{sinc}^2\frac{\omega t}{4}\sin^2\frac{\omega t}{4}\,. \end{aligned} \tag{4}$$

using $\mathrm{sinc}(x) = \sin(x)/x$.

B. Power spectral density and relation to extracted flux noise parameters

The fluxnoise power spectral density is defined as:

$$S_\Phi(\omega) = \int dt\, e^{-i\omega t} \langle \Phi(t)\Phi(0) \rangle\ . \tag{5}$$

Here, we assume it has the following functional form:

$$S_\Phi(\omega) = \frac{A_f}{|f|} + B = \frac{A_\omega}{|\omega|} + B \quad \text{with } A_\omega = 2\pi A_f \tag{6}$$

i.e., a divergent low frequency part with amplitude A and a frequency independent broadband-noise component, characterised by the amplitude B. We define $A = A_f$ with respect to frequency and not angular frequency. This is not done consistently in the literature and can lead to a factor 2π difference in the quoted A values. We can connect this to the above definition of $S(\omega)$ using

$$S(\omega) = (2\pi)^2 D_\Phi^2 S_\Phi(\omega) = \frac{A_\omega}{|\omega|} \quad \text{and} \quad D_\Phi = \frac{\delta f_{01}}{\delta \Phi} \tag{7}$$

We also define the flux-noise sensitivity D_ϕ with respect to frequency but a factor $(2\pi)^2$ is needed to be consistent with the definition of the decay function $\chi(t)$ above. We then insert $S(\omega)$ in Equation 1 making a change of variables $\omega \rightarrow \theta = \omega t$ to arrive at the suggestive form

$$\chi(t) = t^2 \, 8\pi^2 D_\Phi^2 A_f \int_0^\infty d\theta \, \frac{g_n(\theta)}{\theta} + t \, 4\pi D_\Phi^2 B \int_0^\infty d\theta g_n(\theta) \, , \tag{8}$$

which demonstrates that the decay has a quadratic in time (gaussian) part, which stems from the low frequency $1/f$-noise and a linear in time (exponential) part from the high-frequency (broadband noise) components. We get the echo decay constant Γ_Φ^{e} by inserting $g_1(\theta) = \sin^2 \frac{\theta}{4} \operatorname{sinc}^2 \frac{\theta}{4}$ into Equation 8. Evaluation of the integrals yields the two terms

$$\chi(t) = t^2 \, 8\pi^2 D_\Phi^2 A_f \cdot \ln 2 + t \, 4\pi D_\Phi^2 B \cdot \pi \tag{9}$$

In order to describe this with a single decay constant Γ_Φ^{e} the gaussian first term is typically approximated by an exponential decay $\mathrm{e}^{-t^2 \, (2\pi)^2 D_\Phi^2 \, 2A_f \cdot \ln 2} \sim \mathrm{e}^{-t 2\pi D_\Phi \sqrt{2A_f \, \ln 2}}$ (see e.g. Ref. [9]). This finally yields

$$\chi(t)/t = \Gamma_\Phi^{\mathrm{e}} \sim (2\pi)^2 \, B D_\Phi^2 + 2\pi \sqrt{2A_f \, \ln 2} D_\Phi \tag{10}$$

For the evaluation in the main text we have assumed a similar functional form of the dephasing rate

$$\Gamma_\Phi^{\mathrm{e}} = a D_\Phi^2 + b D_\Phi \, . \tag{11}$$

Comparing with Equation 10 and the parameters used the main text, we identify

$$\begin{aligned} A_{\Phi,1/f}^{1/2} &= \sqrt{A_f} = \frac{b}{2\pi \, \sqrt{2 \, \ln 2}} \\ S_{\Phi,\mathrm{BB}}^{1/2} &= \sqrt{B} = \frac{\sqrt{a}}{2\pi} \end{aligned} \tag{12}$$

Our extracted values $A_{\Phi,1/f}^{1/2}$ for the $1/f$ component of the noise are by a factor of $\sqrt(2)$ smaller than those calculated theoretically in Refs. 6, 7, 9, and 10. However, only Ref. [6] defines $A_{\Phi,1/f}^{1/2}$ with respect to frequency while Refs. 6, 7, 9, and 10 use a definition with respect to angular frequency so we would expect our A values to be a factor 2π smaller than theirs. But most of these works omit the factor $1/2\pi$ in Equation 1 which we believe is needed for the correct definition of $\chi(t)$ and would make our values for A_f identical to

A_ω from these works. Our values for $S^{1/2}_{\Phi,\mathrm{BB}}$ would then be expected to be a factor 2π larger than those quoted e.g. in Ref. 6 however we find that our Equation 12 indicates that our extracted values for $S^{1/2}_{\Phi,\mathrm{BB}}$ should in fact be a factor 2 smaller than theirs.

Therefore, when comparing between values from different sources, one needs to be very careful to ensure that the definitions of $\chi(t)$, $S(\omega)$ and $A^{1/2}_{\Phi,1/f}$ are consistent.

C. A note on units

From the definition of the power spectral density of the flux fluctuations $S_\Phi(\omega)$ in Equation 5 we know that $[S_\Phi] = \frac{\Phi_0^2}{\mathrm{Hz}}$. As the unit of the decay rate is $[\Gamma^{\mathrm{e}}_\Phi] = \mathrm{Hz}$, and the unit of the flux-noise sensitivity is $[D_\Phi] = \frac{\mathrm{Hz}}{\Phi_0}$, we find the parameter units of $[\sqrt{a}] = [\sqrt{B}] = \frac{\Phi_0}{\sqrt{\mathrm{Hz}}}$ and $[\sqrt{A}] = [b] = \Phi_0$.

IV. SUPPLEMENTARY METHODS - NOISE SPECTROSCOPY

For the noise spectroscopy measurements we use fast interleaved measurements of Γ_1 and f_{01}, calculated from T_1 decay and Ramsey traces respectively, to track low-frequency fluctuations of these parameters. In total each measurement consists of 10 h of continuous data acquisition, interspersed with short calibrations every 2.5 h to account for long-term parameter drifts. Due to the long measurement duration we were forced to reduce the number of investigated treatments and qubits. For each treatment the number of qubits that we average over is shown in Supplementary Fig. 4 as an inset. Supplementary Figure 4 shows the integrated histograms for the noise spectroscopy measurements where a single point in the histogram is an average over 1000 shots and each shot contains a range of 20 - 40 measurements to determine Γ_1 and f_{01} with good fitting yield. Given an experiment repetition rate of 1 kHz these measurements are thus sensitive only to the low-frequency limit of parameter fluctuations with an upper cut-off of ≈ 0.03 Hz. In the panels of Supplementary Fig. 4 the thicker red line denotes the median of all the integrated histograms for each treatment. From the slope of this median line within the red shaded region (from 25% to 75% of the histogram points) we determine the width of the distribution that is reported in the paper in Fig. 4 and indicated here with red arrows and dashed lines. The slope of the integrated histogram is proportional to the histogram width as reported in Fig. 4 of

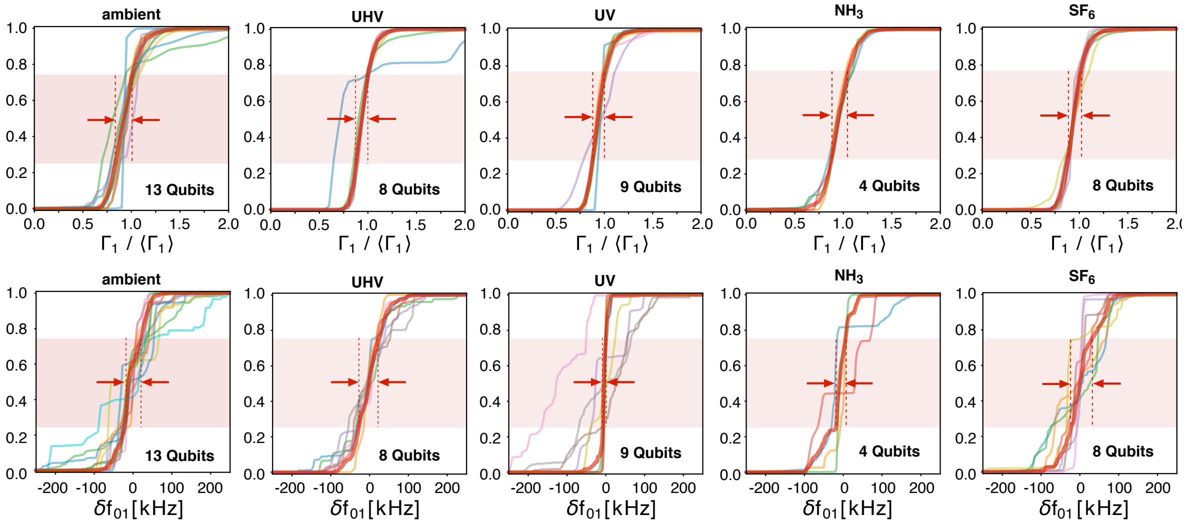

Supplementary Figure 4. Integrated histograms of Γ_1 and f_{01} for each treatment. Arrows indicated the width of distribution which is also reported in Fig. 4 of the main text.

the main text and the maximum median deviation of this slope is given as the error bar in Fig. 4. Compared to a conventional averaged histogram this procedure is less sensitive to outliers. In Supplementary Fig. 4 the top row shows Γ_1 fluctuations normalized by the average Γ_1 for each treatment. The normalization was used in order to allow averaging over qubits with different Γ_1. The second row shows the width of the δf_{01} distribution around the sweet spot of each qubit.

V. SUPPLEMENTARY METHODS - FREQUENCY TUNING USING ION MILLING

As with all the other experiments frequency tuning was performed on flux tunable transmon qubits, and we define the *qubit frequency* f_{01} as the maximum of the fit to the effective qubit frequency vs external flux, i.e. the frequency at the qubit sweet spot with integer flux. The change in qubit frequency Δf_{01} due to the different ion milling conditions listed in Supplementary Tab. II is presented in Fig. 5 of the main text. Ion milling with Ne ions at low ion energy (i) results in an average qubit frequency change of -55 MHz. However, increasing the ion energy of the Ne ions and doubling the ion exposure time (ii) increases the frequency tuning 3-fold to $\Delta f_{01} = 152$ MHz. Replacing the Ne ions with SF_6 ions (iii) reduces the frequency tuning to $\Delta f_{01} = 38$ MHz. Adjusting the distance between the ion source and the qubit plane by a few mm (iv) results in a 3-fold increase in the frequency tuning, i.e. $\Delta f_{01} = 131$ MHz. We expect that ion milling of the qubit junctions leads to a small amount of material removal around the edges. The change in effective junction area calculated with the sputter rate is roughly consistent with the change in qubit frequency. With SF_6 the situation is more complex as the exact composition of the various ion species that is accelerated towards the sample surface is not known. Generally, we expect the ion fragments to be larger than atomic Ne and thus the penetration depth and sputter efficiency to be smaller. As can be seen in Fig. 5 of the main text, frequency tuning with Ne ions has a strong impact on T_1 of the qubits. The average relative change of T_1 for both parameter conditions of frequency tuning with Ne ions, (i) & (ii), is $\Delta T_1 \sim -23\%$. In contrast, frequency tuning with SF_6 ions, (iii) & (iv), leads to no significant relative change of T_1. The statistical variations for the measured T_1 times for all qubit frequency tuning conditions are attributed to cooldown to cooldown variations and T_1 fluctuations. The different impact of ion milling with Ne and SF_6 on T_1 is likely due to the fact that Ne ions can penetrate deeper into the Josephson junction of the qubit [2] leaving vacancies and implanted ions behind that increase the number of TLSs.

To make the link between changes in qubit frequency and junction resistance [11] we measured the impact of the same ion milling treatments on the normal state resistance R_N of single Josephson junctions in arrays of 270 junctions. These measurements were performed with a room temperature probe-station in a two-probe setup. Care was taken to measure the junctions directly after removing the chips from the UHV treatment system in order to minimize effects due to re-oxidation under ambient conditions. Note that these were separate treatment runs since only one UHV package can be loaded in the treatment system at a time and the treatment numbers of the qubit measurements and junction array measurements do not directly correspond to each other. The average starting resistance of

	Label	Gas	U_acc [kV]	t [min]	I_ion [nA]	Details
(i)	Ne	Ne	0.75	20	~ 45	-
(ii)	Ne + NH_3	Ne	1.25	40	~ 47	NH_3 passivation
(iii)	SF_6	SF_6	1.25	20	~ 42	-
(iv)	$2 \times SF_6$	SF_6	1.25	20	~ 45	closer to source

Supplementary Table II. Ion milling conditions for qubit frequency tuning.

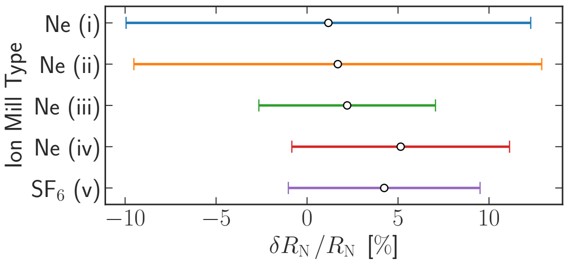

Supplementary Figure 5. Relative change in normal state resistance $\Delta R_\mathrm{N}/R_\mathrm{N}$ of Josephson junctions treated with ion milling. The points represent the mean value and the error bars the standard deviation.

the junctions in the array was $R_\mathrm{N} = 19.4$ kΩ which is lower than that of the individual junctions of the qubit SQUID loops.

Supplementary Figure 5 shows both the mean value and standard deviation of the measured relative changes in R_N after each treatment. Here, treatments (i) through (iv) refer to ion milling parameters with increasing intensity as given in Supplementary Tab. III. At an ion current of 45 nA the ion flux is roughly 1.5×10^{12} ions/cm^2/s. For a 20 min treatment this corresponds to a total ion density of about 15 ions/nm^2. Assuming a roughly linear dependence on ion energy and completely neglecting the different sputter rates of oxides compared to metals [2] we fit the relative change of the normal-state resistance $\Delta R_\mathrm{N}/R_\mathrm{N}$ to an empirical formula given by $\frac{\Delta R}{R} \approx 0.35\ \mathrm{U_{acc}[V]\ t[s]\ I_{ion}[A]}$. The last column in Supplementary Tab. III shows the estimated $\Delta R_\mathrm{N}/R_\mathrm{N}$ using the empirical formula above which is in reasonable agreement with the experimental value in the column to the left even though the uncertainties are large. The last dataset (v) is for SF$_6$ ion milling with similar param-

	Gas	P [mBar]	$\mathrm{U_{acc}}$ [kV]	t [min]	$\mathrm{I_{ion}}$ [nA]	ΔR_N	act. $\Delta R_\mathrm{N}/R_\mathrm{N}$	est. $\Delta R_\mathrm{N}/R_\mathrm{N}$
(i)	Ne	$1.0e^{-4}$	0.75	20	~ 45	240 Ω	1.2%	1.4%
(ii)	Ne	$1.0e^{-4}$	1.0	20	~ 46	362 Ω	1.7%	1.9%
(iii)	Ne	$1.0e^{-4}$	1.25	20	~ 47	532 Ω	2.2%	2.5%
(iv)	Ne	$1.0e^{-4}$	1.25	40	~ 47	1399 Ω	5.1%	5.0%
(v)	SF$_6$	$1.0e^{-4}$	1.25	20	~ 42	1260 Ω	(4.2%)	2.27%

Supplementary Table III. Ion milling conditions for Josephson junction tuning together with actual measured and estimated relative changes in normal state resistance.

eters as for treatment (iii). The measured resistance increase is significantly larger than what we expect from the empirical formula and from our understanding that SF_6 leads to less ion milling compared to neon. As these junction array measurements were done under ambient conditions we speculate that the passivation layer that is left by the SF_6 ion treatment leaves the surface much more hydrophobic and thus increases the effective two-probe resistance that we measure. In contrast to this, we find that the average resistance of the junctions decreases by about 2% if the chips are stored for a couple of days and remeasured without treatment.

The change in R_N of the Josephson junctions due to the ion beam exposure can be used to tune the frequency of transmon qubits, since $f_{01} \propto R_\mathrm{N}^{-\frac{1}{2}}$. Using the *Ambegaokar-Baratoff* relation [11] $I_\mathrm{C} = \frac{\pi\Delta}{2eR_\mathrm{N}}$ and $E_\mathrm{J} = \frac{\hbar I_\mathrm{C}}{2e}$ we find $E_{01} = \sqrt{8E_\mathrm{J}E_\mathrm{C}} - E_\mathrm{C} = R_\mathrm{N}^{-\frac{1}{2}}\sqrt{\frac{h\Delta E_\mathrm{C}}{e^2}} - E_\mathrm{C}$. For small changes we can take the derivative to find $\delta E_{01} = -\sqrt{\frac{1}{4}\frac{R_\mathrm{K}}{R_\mathrm{N}}\Delta E_\mathrm{C}} \cdot \frac{\Delta R_\mathrm{N}}{R_\mathrm{N}}$, with $R_\mathrm{K} = \frac{h}{e^2} \approx 25.8\ \mathrm{k\Omega}$. This then leads to the formula in the main text $\delta f_{01} = -\frac{1}{2h}\sqrt{\Delta \cdot E_\mathrm{C}}\sqrt{\frac{R_\mathrm{K}}{R_\mathrm{N}}\frac{\Delta R_\mathrm{N}}{R_\mathrm{N}}} \approx -1.866\ \mathrm{GHz}\sqrt{\frac{25.8k\Omega}{R_\mathrm{N}}} * \frac{\Delta R}{R_\mathrm{N}}$ with $R_\mathrm{N} = R/2 = 14.5\ \mathrm{k\Omega}$, $\Delta = 172\ \mu\mathrm{eV}$ the superconducting gap of aluminum and $E_\mathrm{C} = h \cdot 335$ MHz the average anharmonicity of the qubits. Because ion milling, i.e. material removal, leads to an increase in Josephson junction resistance, it will therefore result in a decrease in transmon qubit frequency. If we estimate the frequency changes for the neon treatments using the junction data and the formulas above we get a frequency change which is slightly lower but consistent with the measured values in Fig. 5 (a) of the main text.

---

[1] Córcoles, A. *et al.* Demonstration of a quantum error detection code using a square lattice of four superconducting qubits. *Nat. Commun.* **6**, 6979 (2015).

[2] Mergenthaler, M. *et al.* Ultrahigh vacuum packaging and surface cleaning for quantum devices. *Rev. Sci. Instrum.* **92**, 025121 (2021).

[3] Martinis, J. M., Nam, S., Aumentado, J., Lang, K. M. & Urbina, C. Decoherence of a superconducting qubit due to bias noise. *Phys. Rev. B* **67**, 094510 (2003).

[4] Yoshihara, F., Harrabi, K., Niskanen, A. O., Nakamura, Y. & Tsai, J. S. Decoherence of Flux Qubits due to 1/f Flux Noise. *Phys. Rev. Lett.* **97**, 167001 (2006).

[5] Hutchings, M. D. *et al.* Tunable Superconducting Qubits with Flux-Independent Coherence.

Phys. Rev. Appl. **8**, 044003 (2017).

[6] Luthi, F. *et al.* Evolution of Nanowire Transmon Qubits and Their Coherence in a Magnetic Field. *Phys. Rev. Lett.* **120**, 100502 (2018).

[7] Bylander, J. *et al.* Noise spectroscopy through dynamical decoupling with a superconducting flux qubit. *Nat. Phys.* **7**, 565 (2011).

[8] Cywinski, L., Lutchyn, R. M., Nave, C. P. & Das Sarma, S. How to enhance dephasing time in superconducting qubits. *Phys. Rev. B* **77**, 174509 (2008).

[9] Ithier, G. *et al.* Decoherence in a superconducting quantum bit circuit. *Phys. Rev. B* **72**, 134519 (2005).

[10] Braumüller, J. *et al.* Characterizing and optimizing qubit coherence based on SQUID geometry. *Phys. Rev. Appl.* **13**, 054079 (2020).

[11] Ambegaokar, V. & Baratoff, A. Tunneling Between Superconductors. *Phys. Rev. Lett.* **10**, 486–489 (1963).